Available online at www.sciencedirect.com

ScienceDirect

Transportation Research Procedia 70 (2023) 276–283

Transportation Research Procedia

www.elsevier.com/locate/procedia

8th International Electric Vehicle Conference (EVC 2023)

Mechanical characterization and modelling of lithium-ion batteries

D Clerici[a,] *, F Pistorio[a], F Mocera[a] and A Somà[a]

[a]*Department of mechanical and aerospace engineering, Politecnico di Torino, Corso Duca degli Abruzzi 24, Torino, 10129, Italy.*

Abstract

Mechanical phenomena in lithium-ion batteries are one of the main sources of damage, as well as an indicator of battery health and charge. Then, a deep study of these phenomena may improve battery life, management and safety. Mechanical phenomena are caused by the insertion of lithium ions in the microstructure of the electrodes and can be divided into two main categories: stress and degradation of the electrode microstructure, and battery volume change. The stress and fracture behaviour of the electrode microstructure due to lithium intercalation are studied with an electrochemical-mechanical model. Stress intensity factor is computed to assess how current rate and the geometry of the electrode microstructure affect fracture and may reduce the battery life. In addition to stress in the microstructure, lithium insertion causes the swelling of the entire battery. Then, the thickness change of batteries with different chemistries is measured. These measurements carry important information on the battery states and represent an alternative to voltage to extrapolate charge and health states.

Keywords: Lithium ion battery; Experimental mechanics; Fracture mechanics; Electrode damage; Multi-physics modelling.

1. Introduction

Mechanical phenomena play a significant role in the cycle life, management, and safety of lithium ion batteries (LIB). Lithium ions move between the electrodes of opposite polarity and get into their microstucture during operation, to generate the current flow in the external circuit. Mechanical phenomena arise in the microstructure of electrodes because of the insertion of lithium ions in the particles of the active material, as shown in Figure 1. Indeed, lithium ions cause the volume change of the particle, proportionally to their concentration, when they get into the crystalline structure of the active material: greater the concentration of lithium ions, greater the volume deformation of the particle. At the beginning of charge the anode is at its lowest volume, then lithium ions are

* Corresponding author.
E-mail address: davide.clerici@polito.it

2352-1465
10.1016/j.trpro.2023.11.030

extracted from cathode and get into the anode microstructure as soon as the battery is charged. As a consequence, cathode shrinks and anode swells, reaching its greatest volume at the end of charge when (almost) all the available lithium ions are inserted in the anode microstructure. Vice-versa, cathode is at its lowest volume at the end of charge. As a result, there is always an electrode swelling and the other shrinking during the battery operation (with few exceptions). The volume change of the electrodes have a measurable impact on the volume change of the entire battery: the battery generally swells during charge and shrinks during discharge, as the volume change of the anode (graphite in commercial batteries) is greater than the cathode. The battery volume change is detected with different methodologies and sensors: displacement with laser triangulation sensors (Davide Clerici and Mocera, 2021; Clerici, Mocera and Somà, 2022) and touch probes (Rieger *et al.*, 2016; Mohtat *et al.*, 2021), pressure with load cells (Mohan *et al.*, 2014; Dai *et al.*, 2017; Figueroa-Santos, Siegel and Stefanopoulou, 2020; Perez Estevez *et al.*, 2023), strain with fibre optics (Rente *et al.*, 2021; Peng *et al.*, 2022) and strain gauges (Willenberg *et al.*, 2020).

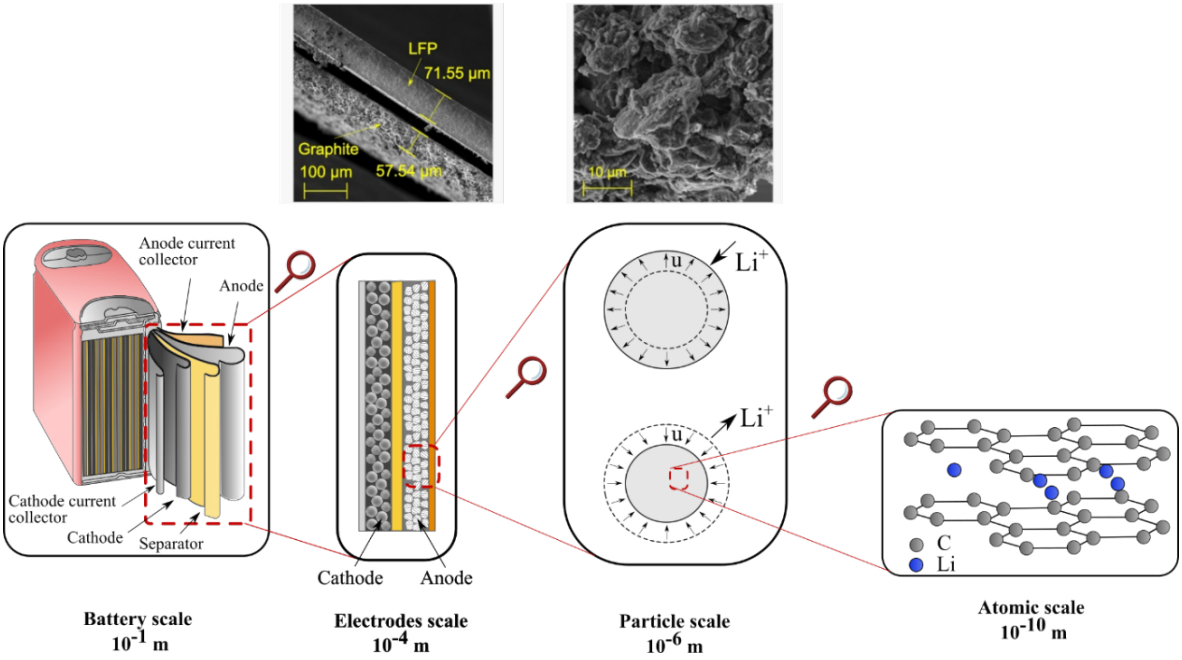

Figure 1. Sketch explaining the multi-physics and mechanical nature of a lithium ion battery. The SEM image on the left shows a couple of electrodes (graphite and LFP), and the one on the right is a magnification of the graphite electrode where the particles are visible. The effect of lithiation and delithiation on the volume change of the particle is shown at the "particle scale". The insertion of lithium ions into the graphite lattice structure is shown at the "atomic scale".

In this work, the volume change of commercial lithium iron phosphate (LFP) and lithium cobalt oxide (LCO) batteries measured during charge and discharge at different current rates is shown. The results show how the LIB volume change can be exploited to estimate its state of charge (SOC) and state of health (SOH).

The lithium ions are not evenly distributed inside the active material particles: they diffuse within the particle, then a greater concentration is present at the particle surface with respect to the core during insertion, and vice-versa during extraction. The uneven concentration distribution causes differential strain, as areas with greater concentration swell more than areas with lower concentration. Differential strain leads to diffusion induced stress (DIS), which ultimately causes the propagation of cracks. Cracks propagation hinders the passage of lithium ions, isolates some portion of active material, and triggers undesired side reactions consuming lithium ions, causing internal resistance rise and capacity fade throughout battery life. In this work, an electrochemical mechanical model is shown, aiming to estimate the stress intensity factor (SIF), which is a scalar quantifying the level of fracture. The influence of operating conditions and the geometry of the electrode microstructure on the SIF is evaluated as well.

Nomenclature

ε_r	Radial strain	R_g	Gas constant	Γ	Contour path
ε_c	Hoop strain	T	Temperature	Λ	Area enclosed in the path
σ_r	Radial stress	F	Faraday constant	x_1	Coordinate direction
σ_c	Hoop stress	I	Current density	x_2	Coordinate direction
σ_h	Hydrostatic stress	R	Particle radius	Γ	Contour path
u	Displacement	r	Radial coordinate	Λ	Area enclosed in the path
c	Concentration	α	Thermal coefficient	D	Diffusion coefficient
ν	Poisson ratio	J_MD	Coupled J-integral	n_i	Normal versor
E	Young modulus	W	Strain energy density	K_I	Stress intensity factor
Ω	Partial molar volume	t_i	Traction vector	t	Time

2. Methodology

2.1. Electrochemical-mechanical and fracture model

The electrochemical-mechanical model aims to compute the concentration distribution of lithium ions in the active material particle due to the lithium flux at its boundary, depending on the current delivered by the battery; afterwards, stress and strain are computed according to the concentration distribution obtained earlier. Table 1 summarizes the main equations of the model (Clerici, Mocera and Somà, 2020a).

Table 1. Equations of the mechanical-diffusive model (Clerici, Mocera and Somà, 2020a). The reader can refer to the list of symbols for the explanation of the symbols used in the equations.

	Mechanical Equations		
Constitutive	$\varepsilon_r = \frac{1}{E}(\sigma_r - 2\nu\sigma_c) + \frac{\Omega c}{3}$	$\varepsilon_c = \frac{1}{E}\left((1-\nu)\sigma_c - \nu\sigma_r\right) + \frac{\Omega c}{3}$	(1)
Congruence	$\varepsilon_r = \frac{\partial u}{\partial r}$	$\varepsilon_c = \frac{u}{r}$	(2)
Equilibrium	$\frac{\partial \sigma_c}{\partial r} = +\frac{2}{r}(\sigma_r - \sigma_c) = 0$		(3)
Boundary conditions	$u\vert_{r=0} = 0$	$\frac{\partial \sigma_r}{\partial r}\vert_{r=R}$	(4)
	Diffusive Equations		
Mass conservation	$\frac{\partial c}{\partial t} = \frac{D}{r^2}\frac{\partial}{\partial r}\left(r^2\frac{\partial c}{\partial r} - r^2\frac{\Omega \bar{c}}{R_g T}\frac{\partial \sigma_h}{\partial r}\right)$		(5)
Boundary conditions	$\begin{cases} \frac{\partial c}{\partial r}\vert_{r=0} = 0, & for\ t \geq 0 \\ \frac{\partial c}{\partial r}\vert_{r=R} = \frac{I}{FD}, & for\ t \geq 0 \end{cases}$	$\begin{cases} c(0,t) = finite, & for\ t \geq 0 \\ c(R,t) = c_R, & for\ t \geq 0 \end{cases}$	(6)
	Solutions		
Displacement	$u(r) = \frac{\Omega}{3(1-\nu)}\left[(1+\nu)\frac{1}{r^2}\int_0^r \bar{c}(r) r^2\, dr + 2(1-2\nu)\frac{r}{R^3}\int_0^R \bar{c}(r) r^2\, dr\right]$		(7)
Radial stress	$\sigma_r(r) = \frac{2\Omega}{3}\frac{E}{1-\nu}\left[\frac{1}{R^3}\int_0^R \bar{c}(r) r^2\, dr - \frac{1}{r^3}\int_0^r \bar{c}(r) r^2\, dr\right]$		(8)
Hoop stress	$\sigma_c(r) = \frac{\Omega}{3}\frac{E}{1-\nu}\left[\frac{2}{R^3}\int_0^R \bar{c}(r) r^2\, dr + \frac{1}{r^3}\int_0^r \bar{c}(r) r^2\, dr - \bar{c}(r)\right]$		(9)

The active material particle is assumed spherical, isotropic and linear elastic, then the problem is one-dimensional thanks to the hypothesis of axisymmetry.

Lithium ions are assumed to diffuse according to the Fickian diffusion model: their flux is proportional to the gradient of concentration (first term of the right-hand side of Equation 5) and by the hydrostatic stress gradient (second term of the right-hand side of Equation 5). The boundary condition of the diffusive problem (Equation 5) depends on the type of battery operation: Galvanostatic operation (first expression of Equation 6) corresponds to a constant lithium flux applied on the particle boundary, and represents constant current operation at the battery scale. Potentiostatic operation (second expression of Equation 6) corresponds to a constant lithium concentration applied on the particle surface, and represents constant voltage operation at the battery scale.

The mechanical field is modeled according to the constitutive (Equation 1), congruence (Equation 2), and equilibrium (Equation 3) equations. The constitutive equation shows that the total deformation is split into the elastic contribution (first term) and the chemical contribution ($\frac{\Omega c}{3}$), depending on the concentration (c). $\boldsymbol{\Omega}$ is the partial molar volume of the host material respect to lithium ions, and tells the strain due to the concentration of one mole of solute. The presence of the chemical contribution to in the constitutive equations makes the mechanical field dependent on concentration, but concentration depends on the hydrostatic stress as well, then the chemical and mechanical fields are coupled.

Traction-free condition is imposed on the outer surface of the particle and the rigid body motion is suppressed by fixing the central point of the particle (Equation 4).

Then, the equilibrium equation is expressed as a function of the displacement u, replacing Equations 1-2 in 3, and integrating the resulting equation twice. The result gives the displacement solution (Equation 7), then the solution of strain and stress is computed replacing the displacement solution into the congruence and constitutive equations, and it is reported in Equations 8-9.

It is pointed out that chemical deformation ($\frac{\Omega c}{3}$), is equivalent to thermal deformation, if $\frac{\Omega}{3}$ is replaced by α and the concentration is replaced by temperature (Clerici, Mocera and Somà, 2020a; D Clerici and Mocera, 2021; Clerici, Mocera and Pistorio, 2022).

Despite the numerous fracture mechanisms reported in the literature according to the specific active material, pre-existent defects in electrode microstructure mainly propagate due to mode-I caused by the tensile hoop stress (Clerici, Mocera and Pistorio, 2022; Pistorio, Clerici and Mocera, 2022).

According to LEFM theory, crack propagation due to a static load occurs when mode-I SIF (K_I) is greater than the fracture toughness, which is a material parameter determined experimentally. K_I is computed from the J-integral, which is equal to the energy release rate when the hypotheses of LEFM theory holds, according to Equation 10.

$$K_I = \begin{cases} \sqrt{\{E\, J_{MD}\}}, & plane\ stress \\ \sqrt{\dfrac{\{E\, J_{MD}\}}{(1-\nu^2)}}, & plane\ strain \end{cases} \tag{10}$$

where J_{MD} is the modified version of path-independent J-integral for coupled mechanical-diffusive problem and its expression is reported in Equation 11 (Pistorio *et al.*, 2023).

$$J_{MD} = \int_{\Gamma} (W dx_2 - \boldsymbol{t} \frac{\partial \boldsymbol{u}}{\partial x_1} ds) + \int_{\Lambda} \Omega \sigma_h \frac{\partial c}{\partial x_1} d\Lambda \tag{11}$$

where Γ is an arbitrary counter clockwise path surrounding the crack tip, W is the strain energy density, $\boldsymbol{t}$ is the traction vector acting on the path Γ with the components equal to $t_i = \sigma_{ij} n_i$, n_i is the versor normal to Γ, Λ is the area enclosed in the path Γ, x_1 is the coordinate direction along the crack extension, x_2 is the coordinate direction perpendicular to the crack extension, and ds is the element length along the path Γ. The additional area integral (second term on the right-hand side of Equation 11) added to the standard J-integral expression developed by Rice (Rice, 1968) (first term on the right-hand side of Equation 11) ensures the path-independence property, accounting for the energy related to the deformation caused by lithium diffusion.

2.2 Battery volume change

The in-operando thickness change of the battery is got measuring the displacement of the battery surfaces (see Figure 2) during charge and discharge with a dedicated test bench. Prismatic graphite/LFP (25 Ah) and pouch graphite/LCO (22 Ah) batteries are tested. The test bench consists of a power supply ‘‘QPX600DP’’ by Aim-TTi, an electronic load ‘‘EL 9080-400’’ by Elektro-Automatik, a thermistor and a couple of laser sensors ‘‘optoNCDT 1900-20’’ by MicroEpsilon for the displacement sensing. The benchmark is controlled in real time by the National Instruments controller ‘‘NI PXIe-8861’’. The displacement sensors have a linearity error of ±2 μm, which is about 2% of the maximum displacement measured by each sensor in these tests. The laser sensors are mounted on a dedicated structure which ensures the perpendicularity between laser beam and cell surface and keeps fixed the cell during the acquisition process, as shown in Figure 2.

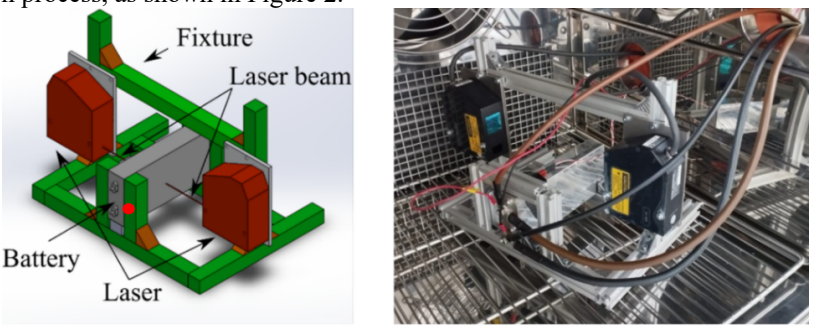

Figure 2. Battery test bench. (a) Conceptualization and (b) realization of the bench for the thickness change measurements with laser sensors during battery operation.

The thickness measurements were carried out in the central point of the larger surfaces, as shown in Figure 2a. Discharge rates range from C/20 up to 2C, and charge just up to C/2. Discharge is carried out with continuous current (CC) until the cut-off voltage (2,5 V for LFP and 3V for LCO), charge begins with CC, when cut-over voltage (3,65 V for LFP and 4,2V for LCO) is reached, a constant voltage is kept until the current drops below C/20. The temperature was kept at 20°C in the climatic chamber during tests.

LIBs temperature rises during operation, proportionally to the current delivered by the battery. Then, both electrochemical processes and temperature changes affect the overall thickness change. LIBs temperature was measured with thermistors simultaneously with thickness change, to identify the thermal contribution to the thickness change measurements. To this end, the thermal deformation coefficient was measured experimentally by changing the temperature inside the climatic chamber (and then LIB temperature) without applying current to the LIB.

3. Results and Discussion

The mechanical phenomena occurring during LIB operation are studied following a twofold approach. First, a fracture mechanics model is built aiming to find the most critical conditions triggering fracture at the electrode microscale. Secondly, the thickness change of LIB is measured experimentally demonstrating how the mechanical phenomena occurring at the microscale affect the macro-scale (Clerici, Mocera and Somà, 2022), according to Figure 1.

3.1 Electrochemical-mechanical problem and fracture

A coupled mechanical-diffusive finite element model (FEM) model is built in Ansys Mechanical APDL for stress and fracture analyses. Graphite is chosen as a case study and its material parameters are: $E = 15$ GPa, $\nu = 0.3$, $\Omega = 3.42 \cdot 10^{-6}\ m^3/mol$, $D = 2 \cdot 10^{-14}\ m^2/s$, $R = 10\ \mu m$ (Clerici, Mocera and Somà, 2020a).

The migration model in Ansys is used to solve for the concentration and stress field simultaneously (Clerici,

Mocera and Somà, 2020b). Then, the coupling between mechanical and diffusive fields is got using coupled field elements with both mechanical and diffusive degrees of freedom, namely PLANE223 for 2D and SOLID226 for 3D model. A detailed description of the mesh as well as the strategy adopted to build the FEM model in Ansys is provided in authors' previous works (Clerici, Mocera and Pistorio, 2022; Pistorio *et al.*, 2023).

Figure 3a shows the distribution of the hoop stress as a function of the particle radius at the end of the lithium extraction process, considering different current rates. The hoop stress changes along the radial coordinate: it gets the lowest compressive value at the particle core (r=0), then it increases and becomes tensile going from the particle core to the surface (r=R). Vice-versa, the hoop stress is compressive on the surface and tensile in the core during lithium insertion. Furthermore, higher current rate corresponds to higher lithium flux at the particle boundary, causing steeper concentration gradient and higher tensile hoop stress ultimately.

Spherical particle with pre-existent superficial cracks is modelled to analyze mode-I fracture caused by tensile hoop stress during lithium extraction, according to the results of the stress analysis. Different particle radii and the current rates are simulated aiming to find the most critical condition triggering fracture.

Figure 3b shows the mode-I SIF as a function of current rate and particle radius due to delithiation. The results shows that K_I keeps a linear trend with respect to the current rate. In addition, larger particles charged (or discharged) at higher current rate are more detrimental from the fracture point of view, resulting in higher hoop stress and K_I values, in agreement with the experimental works (Lin *et al.*, 2017; Hitt *et al.*, 2022).

Furthermore, Figure 3b shows that crack propagation due to a static load is restricted to very high current rate during a single insertion (or extraction), according to the fracture toughness K_{Ic} value of graphite equal to 0.79 Mpa $m^{0.5}$ (Sun, Bhattacharya and Alpas, 2018). As a consequence, mechanical damage due to fracture is more likely to occur during repeated charge/discharge cycles when fracture can be triggered at K_I lower than K_{Ic} due to the fatigue phenomenon.

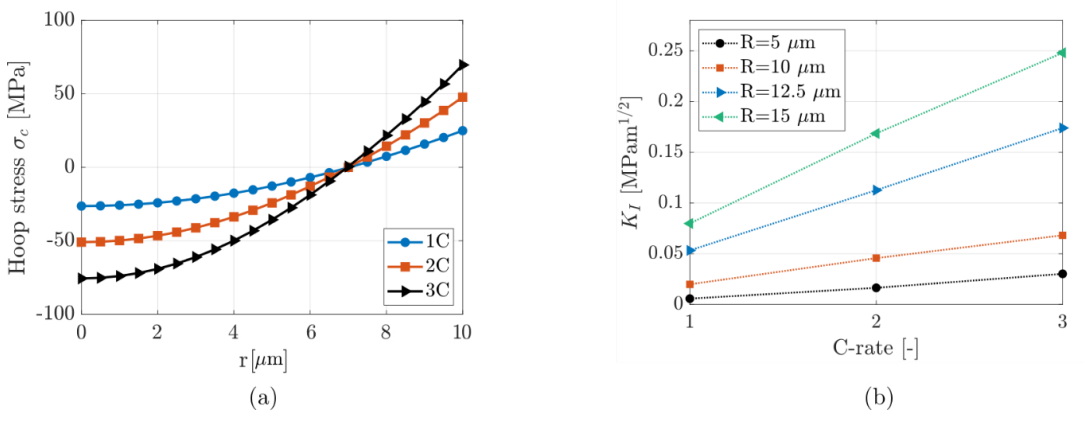

Figure 3. (a) Hoop stress in a 10µm radius graphite particle for different current rates due to delithiation. (b) Stress intensity factor as a function of current rate and particle radius due to delithiation.

3.2 In-operando battery thickness change measurements

LIBs thickness change is the result of the (de)lithiation of the electrode microstructure during operation, then it arises at the microscale and it has a measurable impact on the macroscale (Clerici, Mocera and Somà, 2022), as conceptualized in Figure 1. The results of the thickness change measurements are reported in Figure 4a-b for the LFP-graphite battery and in Figure 4c-d for the LCO-graphite battery. From the results, it is clear how LIBs swell during charge and shrink during discharge. This happens because anode deformation is greater than cathode, then the swelling of the anode is greater than the shrinkage of the cathode when the anode is lithiated and the cathode is delithiated (charge). For the same reason, LIBs shrinks during discharge.

A slight dependence of thickness change on current rate is observed during discharge, especially in the LFP battery. This fact is due to the appearance of phase "IIL" during the graphite delithiation at low current rates. Phase "IIL" gradually disappears increasing the delithiation rate, and does not appear at all during lithiation (Didier *et al.*, 2020), as confirmed by the absence of current rate dependence during charge (Figure 4b,d).

The thickness change of the LIB is quasi-linear for the LFP and linear for the LCO battery with respect to the SOC. Then, it can represent an alternative quantity to estimate SOC instead of voltage. The main advantages with respect to voltage are two: thickness change is not (or substantially less) affected by the applied current, and does not show a plateau, i.e. small change in the measurements does not correspond to large change in SOC. The drawbacks are the influence of temperature on thickness change and the more complex measurement set-up in industrial applications with respect to voltage.

SOH can be estimated as well detecting how the shape of the thickness change curve modifies with LIB aging. The changing of electrode characteristics with aging is reported by differential voltage analysis (DVA) (Bloom *et al.*, 2006), and internal gas releases are observed with LIB aging (Louli, Ellis and Dahn, 2019; Schmitt *et al.*, 2020). Both these phenomena can be detected by thickness change curve and be exploited to quantify the SOH.

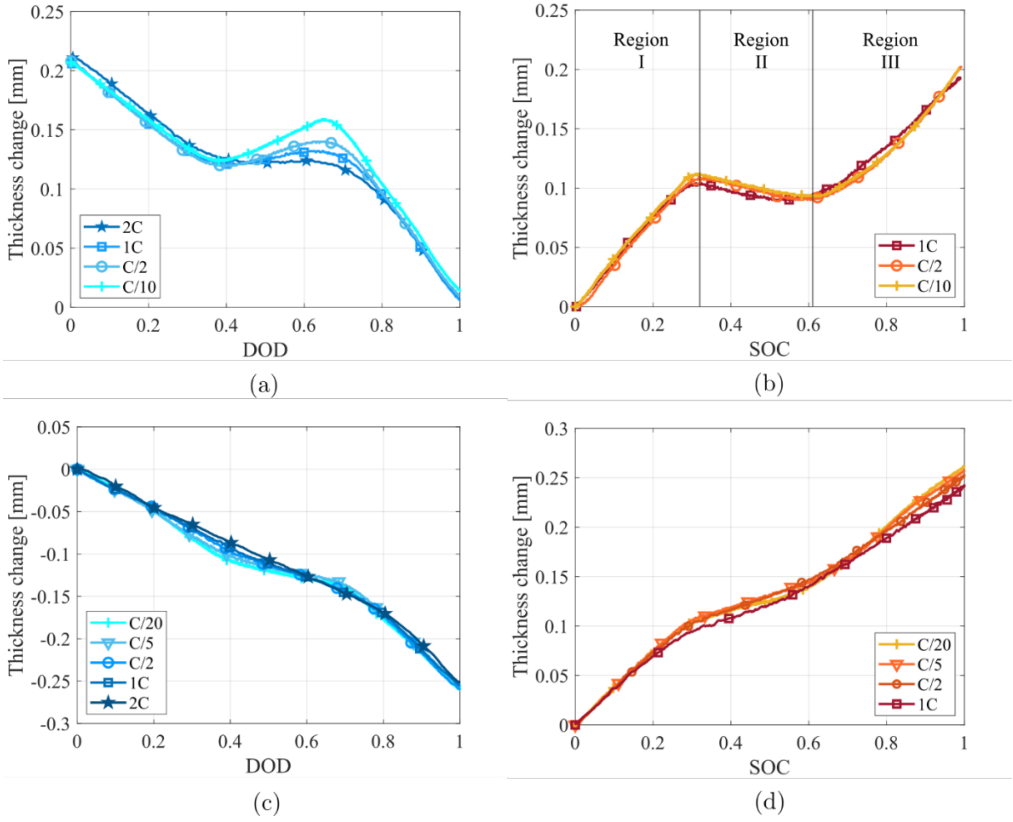

Figure 4. Thickness change measurements of LFP battery during (a) discharge and (b) charge, and LCO during (c) discharge and (d) charge for different current rates.

4. Conclusions

The mechanical phenomena occurring in lithium ion batteries during operation are explained in this work. Mechanics arises from the strain of the electrode microstructure due to the insertion of lithium ions, resulting in two phenomena: (a) Diffusion of lithium ions at the particle level leads to concentration gradient, differential deformation, stress and crack propagation, affecting the battery lifespan. (b) The electrode microstructure deformation has a measurable impact on the volume change of the whole battery at macroscale.

A FEM model is established to compute lithium transport, mechanics and fracture mechanics of the electrode microstructure. The results show that tensile hoop stress in active material particles is the driving force for crack propagation. Fracture is assessed by the stress intensity factor, which is linear with respect to the current rate, and its steepness increases proportional to the particle radius. Then, considering that current rate is a fixed LIB requirement, active material powder made of smaller particles are preferred from the fracture mechanic point of view.

Thickness change measurements show that different batteries, in terms of chemistry and format, has a quasi-linear trend with respect to SOC, making the mechanical measures a candidate for on-line SOC estimation, together with voltage and current. SOH can be valuated as well studying the changes of the thickness change curve with aging.

References

Bloom, I. *et al.* (2006) 'Differential voltage analyses of high-power lithium-ion cells. 3. Another anode phenomenon', *Journal of Power Sources*, 157(1), pp. 537–542. doi: 10.1016/j.jpowsour.2005.07.054.

Clerici, Davide and Mocera, F. (2021) 'Experimental Characterization of Lithium-Ion Cell Strain Using Laser Sensors', *Energies*, 14(19), p. 6281.

Clerici, D and Mocera, F. (2021) 'Micro-scale modeling of Lithium-ion battery', *IOP Conference Series: Materials Science and Engineering*, 1038(1), p. 012007. doi: 10.1088/1757-899x/1038/1/012007.

Clerici, D., Mocera, F. and Pistorio, F. (2022) 'Analysis of fracture behaviour in active materials for lithium ion batteries', *IOP Conference Series: Materials Science and Engineering*, 1214(1), p. 012018. doi: 10.1088/1757-899x/1214/1/012018.

Clerici, D., Mocera, F. and Somà, A. (2020a) 'Analytical solution for coupled diffusion induced stress model for lithium-ion battery', *Energies*, 13(7). doi: 10.3390/en13071717.

Clerici, D., Mocera, F. and Somà, A. (2020b) 'Shape Influence of Active Material Micro-Structure on Diffusion and Contact Stress in Lithium-Ion Batteries', *Energies*, 14(1), p. 134. doi: 10.3390/en14010134.

Clerici, D., Mocera, F. and Somà, A. (2022) 'Electrochemical – mechanical multi-scale model and validation with thickness change measurements in prismatic lithium-ion batteries', *Journal of Power Sources*, 542(March), p. 231735. doi: 10.1016/j.jpowsour.2022.231735.

Dai, H. *et al.* (2017) 'State of charge estimation for lithium-ion pouch batteries based on stress measurement', *Energy*, 129, pp. 16–27. doi: 10.1016/j.energy.2017.04.099.

Didier, C. *et al.* (2020) 'Phase Evolution and Intermittent Disorder in Electrochemically Lithiated Graphite Determined Using in Operando Neutron Diffraction', *Chemistry of Materials*, 32(6), pp. 2518–2531. doi: 10.1021/acs.chemmater.9b05145.

Figueroa-Santos, M. A., Siegel, J. B. and Stefanopoulou, A. G. (2020) 'Leveraging cell expansion sensing in state of charge estimation: Practical considerations', *Energies*, 13(10). doi: 10.3390/en13102653.

Hitt, A. *et al.* (2022) 'Nanotomographic observation and statistical analysis of overcharging induced cracks in LiCoO2 single crystalline particles', *Energy Storage Materials*, 52(August), pp. 320–328. doi: 10.1016/j.ensm.2022.08.011.

Lin, N. *et al.* (2017) 'Understanding the crack formation of graphite particles in cycled commercial lithium-ion batteries by focused ion beam - scanning electron microscopy', *Journal of Power Sources*, 365, pp. 235–239. doi: 10.1016/j.jpowsour.2017.08.045.

Louli, A. J., Ellis, L. D. and Dahn, J. R. (2019) 'Operando Pressure Measurements Reveal Solid Electrolyte Interphase Growth to Rank Li-Ion Cell Performance', *Joule*, 3(3), pp. 745–761. doi: 10.1016/j.joule.2018.12.009.

Mohan, S. *et al.* (2014) 'A Phenomenological Model of Bulk Force in a Li-Ion Battery Pack and Its Application to State of Charge Estimation', *Journal of The Electrochemical Society*, 161(14), pp. A2222–A2231. doi: 10.1149/2.0841414jes.

Mohtat, P. *et al.* (2021) 'Reversible and Irreversible Expansion of Lithium-Ion Batteries Under a Wide Range of Stress Factors', *Journal of The Electrochemical Society*, 168(10), p. 100520. doi: 10.1149/1945-7111/ac2d3e.

Peng, J. *et al.* (2022) 'State estimation of lithium-ion batteries based on strain parameter monitored by fiber Bragg grating sensors', *Journal of Energy Storage*, 52(PB), p. 104950. doi: 10.1016/j.est.2022.104950.

Perez Estevez, M. A. *et al.* (2023) 'Aging estimation of lithium ion cells under real-world conditions through mechanical stress measurements', *Journal of Energy Storage*, 64(June 2022), p. 107186. doi: 10.1016/j.est.2023.107186.

Pistorio, F. *et al.* (2023) 'Review on the numerical modeling of fracture in active materials for lithium ion batteries', *Journal of Power Sources*, 566(March), p. 232875. doi: 10.1016/j.jpowsour.2023.232875.

Pistorio, F., Clerici, D. and Mocera, F. (2022) 'Review on the Experimental Characterization of Fracture in Active Material for Lithium-Ion Batteries', *Energies*, 15(23), p. 9168.

Rente, B. *et al.* (2021) 'Lithium-Ion Battery State-of-Charge Estimator Based on FBG-Based Strain Sensor and Employing Machine Learning', *IEEE Sensors Journal*, 21(2), pp. 1453–1460. doi: 10.1109/JSEN.2020.3016080.

Rice, J. R. (1968) 'A path independent integral and the approximate analysis of strain concentration by notches and cracks', *Journal of Applied Mechanics, Transactions ASME*, 35(2), pp. 379–388. doi: 10.1115/1.3601206.

Rieger, B. *et al.* (2016) 'A New Method to Model the Thickness Change of a Commercial Pouch Cell during Discharge', *Journal of The Electrochemical Society*, 163(8), pp. A1566–A1575. doi: 10.1149/2.0441608jes.

Schmitt, J. *et al.* (2020) 'Measurement of gas pressure inside large-format prismatic lithium-ion cells during operation and cycle aging', *Journal of Power Sources*, 478(June), p. 228661. doi: 10.1016/j.jpowsour.2020.228661.

Sun, G., Bhattacharya, S. and Alpas, A. T. (2018) 'Cyclic strain-induced crack growth in graphite during electrochemical testing in propylene carbonate-based Li-ion battery electrolytes', *Journal of Materials Science*, 53(2), pp. 1297–1309. doi: 10.1007/s10853-017-1547-y.

Willenberg, L. K. *et al.* (2020) 'High-Precision Monitoring of Volume Change of Commercial Lithium-Ion Batteries by Using Strain Gauges', *Sustainability*\, 12(2), p. 557.